Role of electronic correlations in room-temperature ferromagnetism of monolayer MnSe$_2$

Jeonghoon Hong,[1] Chang-Jong Kang [2,3,*] and Jeongwoo Kim [1,4,*]

[1]*Department of Physics, Incheon National University, Incheon 22012, Korea*
[2]*Department of Physics, Chungnam National University, Daejeon 34134, Korea*
[3]*Institute of Quantum Systems, Chungnam National University, Daejeon 34134, Korea*
[4]*Intelligent Sensor Convergence Research Center, Incheon National University, Incheon 22012, Korea*

The electronic structure of a two-dimensional ferromagnetic MnSe$_2$ monolayer was investigated using density functional theory. It was found that the computed Curie temperature (T_C), which is fairly high but lower than room temperature, is sensitive to the on-site Coulomb repulsion U, indicating that electronic correlations have an important role in the magnetism exhibited in the system. The primary exchange mechanism responsible for the large T_C of monolayer MnSe$_2$ was also clarified. Furthermore, it was demonstrated that the T_C can be enhanced up to nearly room temperature through charge doping and heterostructure engineering. These findings not only provide a fundamental understanding of the mechanism of magnetic ordering in MnSe$_2$ monolayers, but also suggest a practical remedy for the enhancement of the T_C of MnSe$_2$ by using various substrates, including Dirac materials.

I. INTRODUCTION

The search for new two-dimensional (2D) magnetic materials is important because they have promising applications in spintronic devices [1–4]. Since monolayer Cr$_2$Ge$_2$Te$_6$ was mechanically exfoliated several years ago [5], various 2D magnets have been discovered [6–10]. Fe$_3$GeTe$_2$ was found to have topological nodal lines depending on its spin orientation [11], and various Fe-based van der Waals (vdW) ferromagnets, such as Fe$_4$GeTe$_2$ and Fe$_5$GeTe$_2$, have been studied [12,13]. Atomically thin CrI$_3$ layers, unlike the ferromagnetic (FM) bulk phase, possess antiferromagnetic (AFM) interlayer coupling determined by the stacking configuration [14,15], which can be electrostatically controlled [16–18]. Furthermore, 2D AFM materials, such as FePS$_3$ [19], MnP$_3$ [20], CrCl$_3$ [21], and NiPS$_3$ [22] have attracted significant interest because unexplored quantum phenomena can be induced by the coexistence of many-body quasiparticles and AFM magnetic order in the reduced dimension [23]. Recently, a type-II multiferroic order with a proper-screw spin helix was realized in a single layer of NiI$_2$ [24].

Despite the intriguing electronic and magnetic properties of low-dimensional magnetic systems, 2D magnetism mostly occurs at very low temperatures, which limits their practical application at room temperature. For example, the Curie temperatures (T_C) of Cr$_2$Ge$_2$Te$_6$ and CrI$_3$ are 61 and 45 K, respectively, which are far below room temperature. Therefore, a high T_C is a prerequisite for the utilization of 2D magnetic materials in device applications. In this respect, 1T-MnSe$_2$, which is grown on the surface of the α-MnSe bulk, is a promising candidate for room-temperature device

applications, as well as VSe$_2$ [8] and CrTe$_2$ [25]. The stability of the atomic and magnetic structures of monolayer MnSe$_2$ has been theoretically examined [26,27], and an increase in T_C by strain and defect was predicted [28–30]. However, the relationship between electronic correlations and magnetism has not been systematically investigated in single-layer MnSe$_2$. For the bulk α−MnSe phase, the calculated electronic structure is well matched with experiments when the on-site Coulomb repulsion parameter U for the Mn d orbital is considered [31]. The high T_C of the MnSe$_2$ monolayer is also successfully reproduced by considering a significant U value for Mn atoms [27], implying the importance of the correlation effect for a fundamental understanding of the microscopic origin of room-temperature magnetism.

In this paper, the role of electronic correlations in the electronic and magnetic properties of a 2D FM MnSe$_2$ monolayer was investigated using density functional theory (DFT) calculations. The T_C of MnSe$_2$ was computed, and it was found that it varies strongly with the on-site Coulomb repulsion parameter U, indicating that electronic correlation is an important factor in describing the magnetic properties of the MnSe$_2$ monolayer. The appropriate U value of MnSe$_2$ was determined by taking the hybrid functional result as a reference. The relationship between T_C and some easily achievable variations—charge doping (electrons or holes) and heterostructure engineering with substrates of graphene, GaSe, and Bi$_2$Te$_3$ (BT)—was further explored. It was found that any type of charge doping can lead to a large increase in T_C and that the mechanism of the exchange reinforcement can vary depending on the substrate. The findings not only widen the fundamental understanding of 2D magnetic materials, but also provide a convenient method for enhancing T_C.

*Corresponding author: cjkang87@cnu.ac.kr; kjwlou@inu.ac.kr

II. METHOD

DFT calculations were performed using the projected augmented plane-wave method [32,33] implemented in the Vienna *ab initio* simulation package [34]. The generalized gradient approximation (GGA) of Perdew-Burke-Ernzerhof (PBE) [35] was adopted for the exchange-correlation functional. To consider the electronic correlation effect, the Hubbard-U correction (GGA + U method) [36,37] was used for the Mn $3d$ orbitals. Hybrid functional calculations devised by Heyd, Scuseria, and Ernzerhof (HSE) [38,39] were also performed, and it was found that the GGA + U scheme with $U = 3$ eV reproduced the HSE results well. An energy cutoff of 400 eV was used for the plane-wave basis. The energy convergence threshold for the self-consistent solution of the Kohn-Sham equations was set at 10^{-5} eV. A dense $41 \times 41 \times 1$ **k**-point mesh was used to sample the entire Brillouin zone. To avoid interactions between the layers, a vacuum distance of 20 Å was added in the direction normal to the 2D plane. The atomic structure and lattice parameters were fully relaxed, preserving lattice symmetry until the total energy was less than 10^{-4} eV. The DFT-D2 scheme [40] for dispersion correction was employed to describe the vdW interactions between the MnSe$_2$ layer and the substrates. To calculate the orbital-resolved exchange parameters, the WANNIER90 [41] and TB2J codes [42] were utilized. An extended tight-binding model was constructed by mapping the resulting DFT wave functions onto Wannier functions [43]. The Wannier functions of MnSe$_2$ were constructed from the initial projections of the Mn $3d$ and Se $4p$ bands in the relevant energy range. Spin-orbit coupling (SOC) yielded no notable differences in the electronic band structures; thus, the SOC effect was not included in the calculations unless otherwise stated in the text of this article.

To obtain T_C, magnetic exchange couplings were first estimated using the following spin Hamiltonian:

$$H_{\text{spin}} = -\sum_{i \neq j} J \, \vec{S}_i \cdot \vec{S}_j,$$

where J is the exchange interaction between two Mn sites (i, j), and $\vec{S}_i$ is the magnetic moment at Mn site i. In this paper, J was computed from the total energy differences for several magnetic configurations. To extract relevant exchange couplings, such as the nearest- (J_1), next-nearest- (J_2), and third-nearest- (J_3) neighbor exchange couplings, a $3\sqrt{3} \times 3\sqrt{3}$ supercell of the MnSe$_2$ monolayer was adopted to compute the total energy differences. The exchange coupling is obtained using the following formula [44]:

$$J = \frac{E_1 + E_4 - E_2 - E_3}{4(\vec{S}_i \cdot \vec{S}_j)}, \quad (1)$$

where E_1, E_2, E_3, and E_4 are the total energies for the spin configurations up-up, up-down, down-up, and down-down at the i and j sites, respectively. Note that a $3\sqrt{3} \times 3\sqrt{3}$ ($2\sqrt{3} \times 2\sqrt{3}$) supercell of the MnSe$_2$ monolayer was adopted to minimize the lattice mismatch in the MnSe$_2$/graphene and MnSe$_2$/GaSe (MnSe$_2$/BT) heterostructures. For the $3\sqrt{3} \times 3\sqrt{3}$ supercell, we renormalized the exchange constant J_4 (J_5) by dividing by a factor of 2 (3) to avoid the overcounting issue.
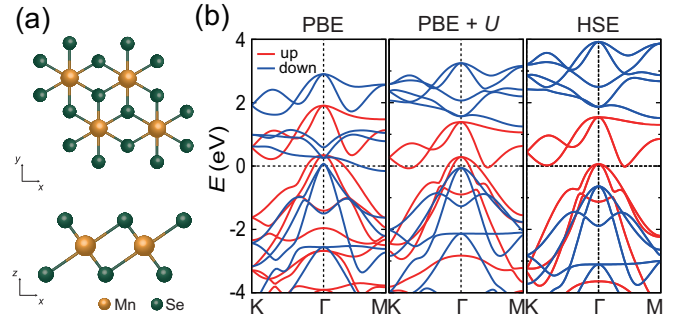
FIG. 1. (a) Top and side views of the atomic structure of a MnSe$_2$ monolayer. Mn and Se atoms are denoted by yellow and green spheres, respectively. Mn atoms form a hexagonal lattice. (b) From the left to right panels, the spin-polarized band structures of the MnSe$_2$ monolayer computed with PBE, PBE + U (3eV), and HSE methods. Up- and down-spin states are represented by red and blue lines, respectively. The Fermi level is set to zero.

Using the obtained J values, T_C is computed within the mean-field level using Eq. (2),

$$T_C = \frac{2S(S + 1)}{3k_B} \sum_i z_i J_i, \quad (2)$$

where S and z_i denote the size of the magnetic moment and the number of nearest-neighboring magnetic atoms for the ith one, respectively. Note that the computed T_C is comparable to the one from Monte Carlo simulations [27,29], thereby confirming that the mean-field approach is sufficient to obtain the T_C in this system.

III. COMPUTATIONAL RESULTS

A. Electronic and magnetic properties of the MnSe$_2$ monolayer

A 1T-MnSe$_2$ monolayer with C_3 symmetry can be realized on the (111) surface of cubic (α-phase) MnSe thin films [45]. As shown in Fig. 1(a), an Mn atom is coordinated by six Se atoms and has an edge-sharing octahedral structure. It forms a honeycomb lattice in the same plane. For bulk α-MnSe, the relaxed lattice constant with the GGA (PBE) potential ($a_{\text{eq}} = 5.37$ Å) better explains the experimental lattice constant ($a_{\text{exp}} = 5.46$ Å) [46] than that with the local-density approximation functional ($a_{\text{eq}} = 5.07$ Å). Therefore, in the calculations, the GGA potential is chosen to describe the atomic and electronic structures of the monolayer MnSe$_2$. The static correlation effect for Mn $3d$ orbitals is also considered using the HSE hybrid functional [7,8] and the DFT + U scheme [36,37]. The relaxed lattice constant of monolayer MnSe$_2$ obtained from the GGA potential is 3.47 Å, and it increases to 3.61 and 3.62 Å with the HSE functional and GGA + U ($U = 3$ eV), respectively.

The band dispersion of the MnSe$_2$ monolayer was calculated to investigate the correlation effect on its electronic structure as shown in Fig. 1(b). The selected U value (3 eV) reproduces not only the HSE atomic structure, but also the electronic structure—particularly, the energy splitting between the spin-up and spin-down states. The PBE potential describes the substantial band overlap between spin-up and spin-down states in the energy window above the Fermi
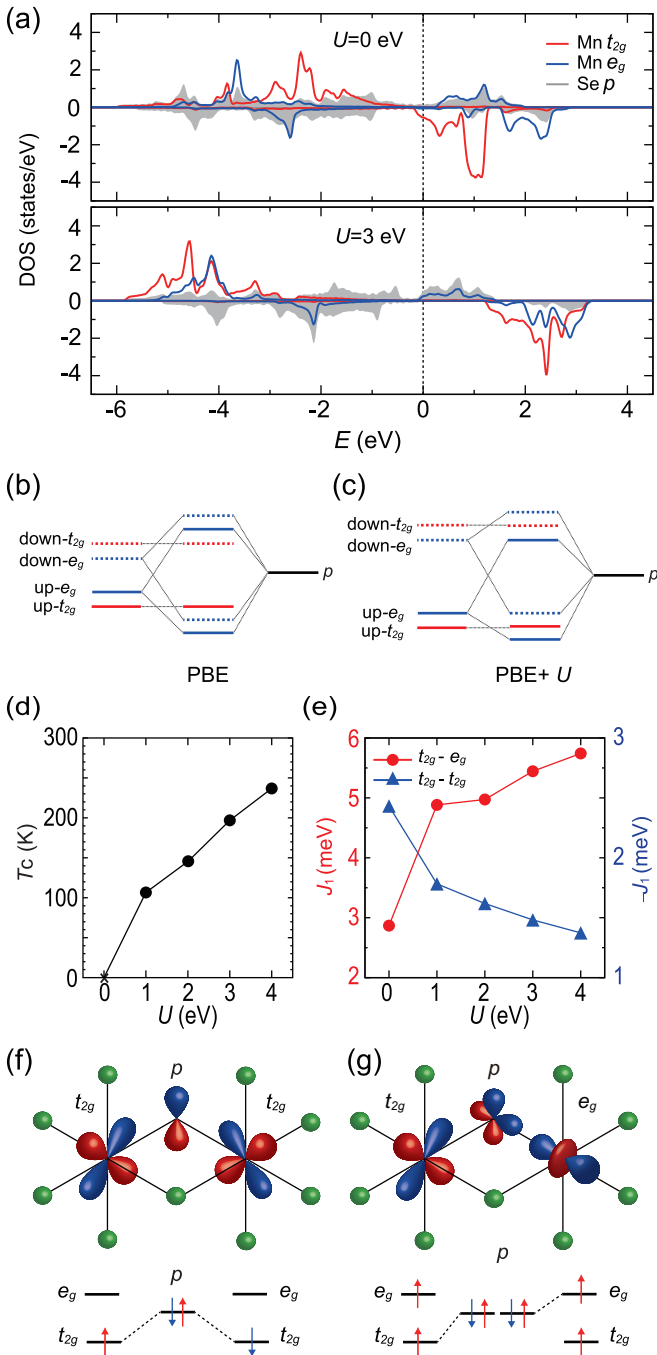
FIG. 2. (a) The orbital-projected density of states of the MnSe₂ monolayer for $U = 0$ and 3 eV. Schematic energy of the MnSe₂ monolayer (b) without and (c) with the U effect. (d) The variation of the Curie temperature (T_C) of the MnSe₂ monolayer as a function of U. (e) The nearest-neighbor exchange constant J_1 as a function of U. The positive sign corresponds to FM coupling. Red circles and blue triangles denote t_{2g}–e_g and t_{2g} – t_{2g} channels, respectively. Schematics of (f) the AFM (t_{2g} – t_{2g}) and (g) the FM (t_{2g}–e_g) exchange coupling between occupied Mn states mediated though Se p orbitals.

correlations could be crucial for the large T_C of the MnSe₂ monolayer. By taking a reference of the HSE functional calculation, the GGA + U ($U = 3$ eV) was finally chosen to investigate the electronic structure of monolayer MnSe₂.

The U effect on T_C was examined to elucidate the relationship between the correlation effect and magnetism in monolayer MnSe₂. In particular, to understand the development of the local magnetic moments of the Mn d orbitals, the variation in the density of states (DOS) of MnSe₂ with the U value was examined—see Fig. 2(a). The fivefold Mn d orbitals split into threefold t_{2g} and twofold e_g states according to the cubic crystal field as shown in the energy diagram in Fig. 2(b). Without U ($U = 0$ eV), the Mn d and Se p orbitals are very close in energy, leading to strong hybridization between the Mn e_g and the Se p states. As a result, for each spin component, the Mn t_{2g} states are located between the bonding and the antibonding e_g states. However, with U ($U = 3$ eV), the Mn d and Se p orbitals are separated in energy, and the hybridization between Mn e_g and Se p states becomes weaker. It diminishes the bonding and antibonding e_g characteristics, and the atomic t_{2g} and e_g levels are, thus, identified relatively well as shown in Figs. 2(a) and 2(c). The spread of t_{2g} and e_g states decreases as the U value increases, demonstrating the localization of Mn d electrons.

Because the electronic structure is sensitive to the U value as shown in Fig. 2(a), T_C is also strongly affected by U—see Fig. 2(d). Interestingly, the AFM order between the two nearest Mn atoms is preferred if U is not considered ($U = 0$), whereas the FM state emerges with finite U values. This indicates that considering the electronic correlations properly is
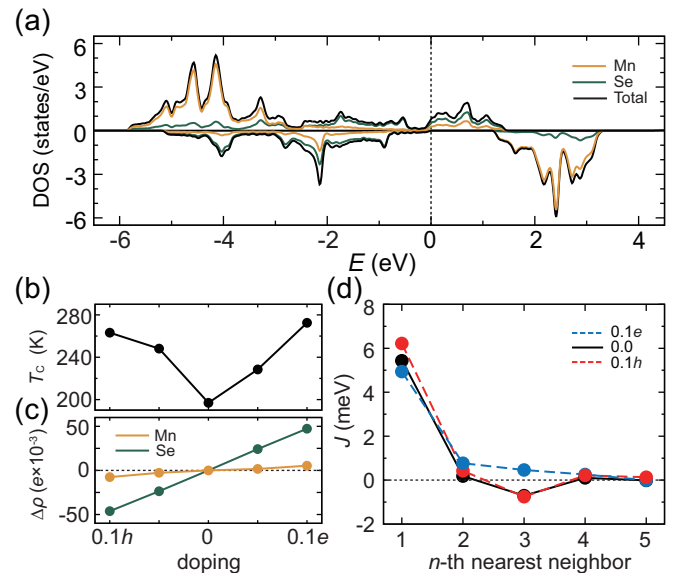
FIG. 3. (a) The atomic projected density of states of the MnSe₂ monolayer computed within the GGA (PBE) + U($= 3$ eV) scheme. (b) The calculated Curie temperature (T_C) of the MnSe₂ monolayer with electron/hole doping. (c) The charge difference of Mn and Se atoms in the MnSe₂ monolayer upon electron/hole doping. (d) The calculated exchange constant (J) as a function of the inter-Mn distance for various doping cases: -0.1 (blue), 0 (black), and 0.1 (red) e/cell. The positive sign in the y axis corresponds to FM coupling.

level, whereas PBE + U and HSE separate spin-up and spin-down bands nearly completely in the same energy window. Therefore, there is a close relation between the spin splitting and the electronic correlations, implying that the electronic
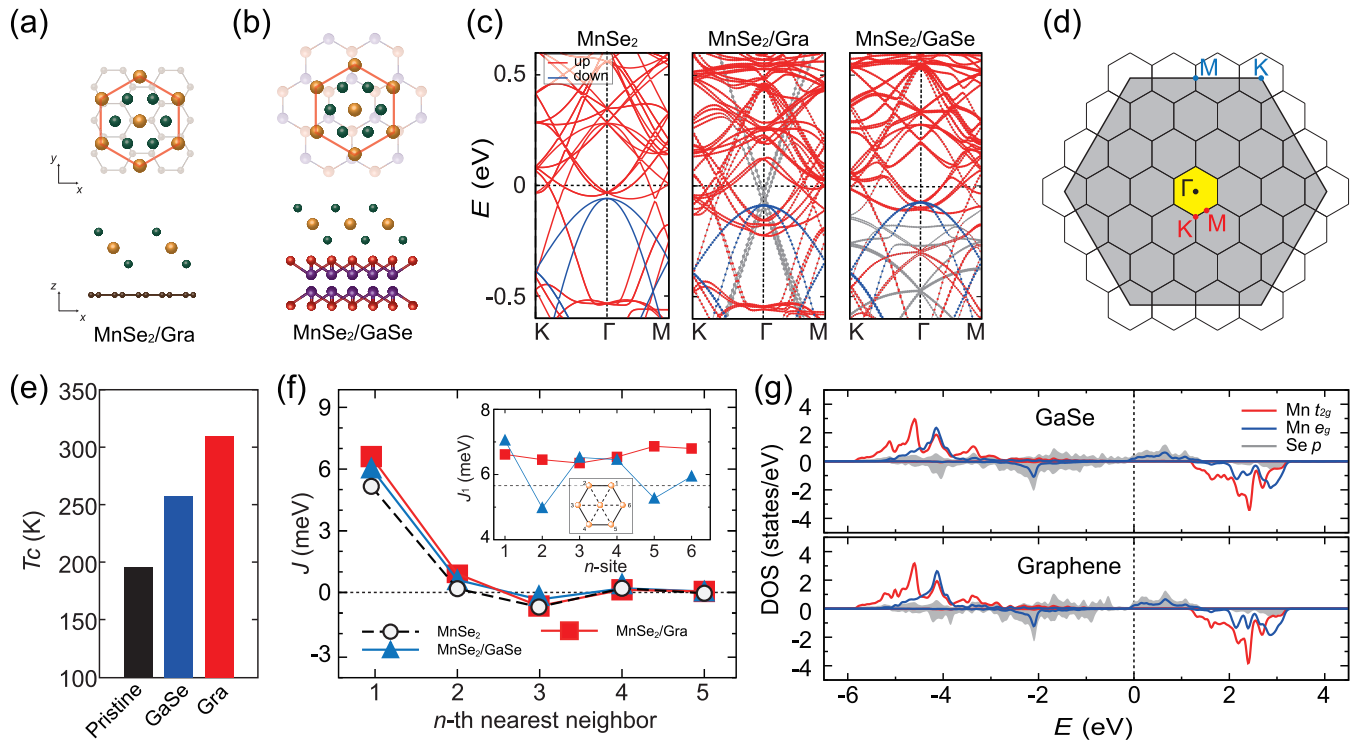
FIG. 4. Top and side views of the atomic structure of (a) $MnSe_2$/graphene and (b) $MnSe_2$/GaSe. The substrate C, Ga, and Se atoms are denoted by brown, purple, and red spheres, respectively. (c) The $MnSe_2$-projected band structure with spin resolution for pristine $MnSe_2$, $MnSe_2$/graphene, and $MnSe_2$/GaSe. Up- and down-spin states of $MnSe_2$ are represented by red and blue lines, respectively. The weight of graphene or GaSe is represented by gray lines. The Fermi level is set to zero energy. All band dispersions are presented in the Brillouin zone of the $3\sqrt{3} \times 3\sqrt{3}$ expanded cell shown in (d). (d) Brillouin zones for the primitive cell (gray) and $3\sqrt{3} \times 3\sqrt{3}$ expanded cell (yellow) of $MnSe_2$ for the heterostructure calculations (e) The calculated Curie temperature (T_C) of pristine $MnSe_2$, $MnSe_2$/graphene, and $MnSe_2$/GaSe. (f) The calculated average exchange constant (J) of pristine $MnSe_2$, $MnSe_2$/graphene, and $MnSe_2$/GaSe as a function of the inter-Mn distance. The inset represents inequivalent J_1 values for six different Mn sites in the $MnSe_2$ monolayer placed on the substrates. (g) The orbital-projected density of states of $MnSe_2$/graphene and $MnSe_2$/GaSe. The Fermi level is set to zero energy.

of great importance for appropriately describing the magnetic properties of the $MnSe_2$ monolayer. The FM order becomes stronger owing to the U effect, and the T_C increases with U. The AFM and FM contributions were extracted from the total exchange interaction using the Green's function method [47]. Similar to other 2D magnets driven by the superexchange mechanism where local magnetic moments are mediated by anion p orbitals [48–52], the FM (AFM) coupling primarily comes from t_{2g}–e_g ($t_{2g} - t_{2g}$) hopping channels, which significantly increase (decrease) with increasing U value as shown in Fig. 2(e).

The suppression of AFM ordering could be interpreted as an energy separation between the states involved in the magnetic channel. Because electron hopping between the Mn t_{2g} and Se p states is responsible for the AFM coupling as shown in Fig. 2(f), the energy difference is a decisive factor in determining the size of the AFM exchange constant. By increasing the U value, the energy separation between the Mn t_{2g} and the Se p orbitals increases, and the corresponding hopping is suppressed. Unlike the AFM exchange channel, the FM channel is mediated by two Se p orbitals where the two p orbitals are coupled using Hund's rule—see Fig. 2(g). Because the occupied Mn t_{2g} and e_g states become closer in energy by the U effect as shown in Fig. 2(a), the FM exchange channel becomes intensified by the increase in U. The

results again demonstrate the importance of the correlation effect in the electronic and magnetic properties of monolayer $MnSe_2$.

Furthermore, the variation of the electronic and magnetic properties was investigated over a wide range of electron/hole doping concentrations. As shown in Fig. 3(a), which presents the electronic structure without charge doping, the metallic states near the Fermi level are mostly derived from the Se states (green line). A direct exchange interaction induced by the wave-function overlap between two adjacent Mn $3d$ orbitals is likely to be marginal because the inter-Mn distance is relatively large (3.62 Å). The computed T_C is presented as a function of the doping concentration ranging from -0.1 to $0.1 e/$cell—see Fig. 3(b). The calculated T_C of monolayer $MnSe_2$, unlike in the experiment [45], is far below room temperature (197 K) as in Fig. 2(d), which is in agreement with previous studies [27,30]. Both electron and hole dopings enhance the T_C up to approximately 280 K as shown in Fig. 3(b); thus, moderate charge doping could be an essential ingredient for the room-temperature 2D magnet. Despite the large variation in the T_C, the local charge density of the Mn $3d$ orbital is almost independent, whereas that of the Se $4p$ orbital changes significantly depending on the doping concentration—see Fig. 3(c). This indicates that the Se $4p$ orbital plays an important role in mediating the local magnetic

moments (mainly attributed to the Mn $3d$ orbital) through the indirect magnetic exchange interaction.

Figure 3(d) shows the exchange constants J of Mn atoms as a function of the inter-Mn distance for electron-/hole-doped $MnSe_2$. Regardless of the doping concentration, the nearest-neighbor exchange constant J_1 is positive (corresponding to FM ordering) and dominates all long-range exchange interactions, indicating that FM is strong and robust, even for charge doping. The exchange constant J rapidly decreases when the inter-Mn distance increases. For 0.1-hole-doped $MnSe_2$, all exchange constants J_i except for the nearest J_1 do not change significantly. The nearest J_1 increases appreciably, which enhances the T_C. However, in the case of 0.1-electron doping per unit cell, the nearest J_1 decreases, but the third J_3 increases significantly. The large enhancement of the third-nearest J_3 results in the growth of T_C despite the reduction of the nearest J_1.

B. Application: heterostructure engineering for the $MnSe_2$ monolayer

The effect of substrates on the large magnetic exchange interaction (T_C) of monolayer $MnSe_2$ was explored further. Two vdW materials were examined as substrates for monolayer $MnSe_2$: graphene as shown in Fig. 4(a), which is widely utilized as a building block for vdW heterostructures [53], and GaSe, as shown in Fig. 4(b), which was used in an experiment to realize $MnSe_2$ [45]. Figure 4(c) shows the spin-resolved electronic structures of monolayer $MnSe_2$ without and with the substrates. A $3\sqrt{3} \times 3\sqrt{3}$ enlarged supercell was used to simulate the heterostructures, leading to a smaller Brillouin zone—see Fig. 4(d). It clearly shows that the projected band structure of monolayer $MnSe_2$ is maintained near the Fermi level, even in the presence of substrates. For the $MnSe_2$ monolayer in proximity to the substrates, the exchange couplings J are no longer equivalent to those for the pristine $MnSe_2$ monolayer because of the in-plane symmetry breaking induced by the substrates—see Figs. 4(a) and 4(b). Therefore, the inequivalent exchange couplings were computed individually to estimate the T_C of the heterostructures. The T_C values of monolayer $MnSe_2$ increased by 25% and 50% in proximity to the GaSe and graphene substrates, respectively—see Fig. 4(e).

To elucidate the origin of the T_C enhancement, the averaged J values were plotted as a function of the inter-Mn distance as shown in Fig. 4(f). For $MnSe_2$/graphene, the large enhancement in T_C is ascribed to a relatively large increase in J_1 and J_2. In the case of the $MnSe_2$/GaSe heterostructure, the equidistant exchange constants change significantly depending on the position of the Mn atoms as shown in the inset of Fig. 4(f), whereas, the change in the equidistant exchange constants is relatively small for the graphene heterostructure. The contrasting behaviors indicate that the substrate effect of graphene is relatively uniform and short range, whereas that of GaSe depends on the details of the stacking geometry between GaSe and $MnSe_2$.

An analysis of the electronic structure also provides important information for understanding the large enhancement of the T_C. For $MnSe_2$/GaSe, the Se-p states (gray area) are somewhat extended near the Fermi level as shown in Fig. 4(g) because of the weak hybridization between the
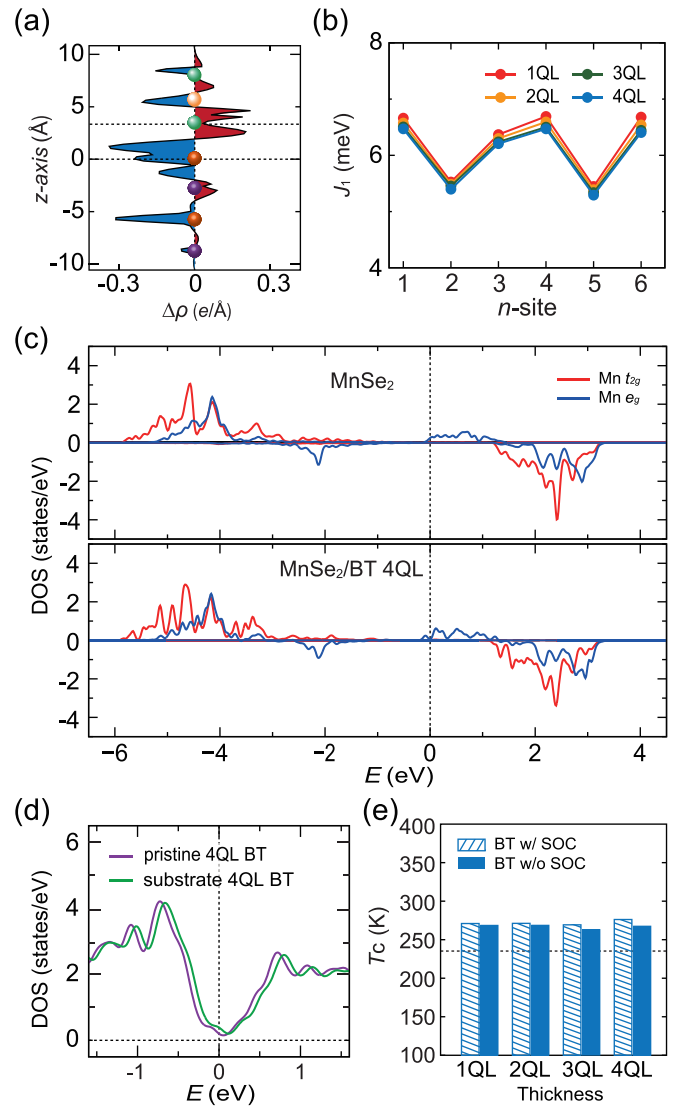
FIG. 5. (a) Line profile of the planar charge difference ($\Delta\rho = \rho_{total} - \rho_{MnSe_2} - \rho_{Bi_2Te_3}$) caused by the interfacial contact of $MnSe_2$ and four quintuple layer (4-QL) BT. The positive (negative) value indicates the charge accumulation (depletion) induced by the proximity of the two systems. Green, yellow, orange, and purple spheres denote Se, Mn, Te, and Bi atoms, respectively. (b) The variation of the inequivalent J_1 values for six different Mn sites in the $MnSe_2$ monolayer depending on the BT thickness. (c) The orbital-projected density of states of pristine $MnSe_2$ (top) and $MnSe_2$/BT (bottom). (d) The calculated density of states of 4-QL BT with and without an adjacent $MnSe_2$ layer. (e) The calculated Curie temperatures (T_C) of $MnSe_2$/BT with varying BT thickness. The T_C estimated with (without) SOC is marked by the colored bars with (without) a line pattern. The black-dashed horizontal line indicates the T_C of pristine $MnSe_2$.

valence bands and the substrate as shown in Fig. 4(c), implying a new superexchange channel through the substrate as realized in bilayer CrI_3 [14,54] and magnetically doped topological insulators [55,56]. Because the interlayer superexchange channel is closely related to the configuration of the Se–Se vdW layers [57], J_1 varies considerably depending on the Mn position as shown in the inset of Fig. 4(f). In contrast,

as already mentioned, the $MnSe_2$/graphene heterostructure depends less on the stacking configuration. The fact that the long-range exchange constants (J_3–J_5) remain intact indicates the absence of an additional exchange channel through the graphene substrate. The $n-$doped graphene Dirac cones— gray dots in Fig. 4(c)—indicate that the graphene accepts a small number of electrons from the $MnSe_2$ layer without significantly changing the electronic structure of the magnetic layer as shown in Figs. 4(c) and 4(g). As a result, the FM superexchange interaction in $MnSe_2$ is strengthened as shown in the hole-doped $MnSe_2$ layer—see Fig. 3(d). Therefore, the substrate effect is another crucial component of the large magnetic exchange interaction.

Because of the obvious substrate effect on the T_C of $MnSe_2$, it was decided to examine whether a further increase in the exchange coupling can be realized by the proximity of a topological surface state (TSS) because TSSs can act as a robust exchange channel between localized magnetic moments [58,59]. The $MnSe_2$/BT heterostructures, which were expanded to $2\sqrt{3} \times 2\sqrt{3}$ supercells on the lateral plane, were calculated to investigate the effect of a topologically insulating substrate. Owing to the different sizes of the supercells adopted in the $MnSe_2$/BT calculations, the electronic/magnetic properties of pure $MnSe_2$ were recalculated for comparison. As shown in the charge-density difference in Fig. 5(a), the interfacing Se atoms gain electrons (red areas around the green spheres) from the topological insulating BT. Similar to the $MnSe_2$/GaSe heterostructure, J_1 between neighboring Mn atoms clearly depends on the Mn position, and the variation is insensitive to the BT thickness—see Fig. 5(b). In other words, J_1 is affected by the stacking geometry between the interfacing $MnSe_2$ and BT layers, indicating the existence of a secondary exchange channel through the substrate BT layers. Despite the influence of BT on $MnSe_2$, the major alteration of the electronic structure caused by BT is not appreciable as shown in Fig. 5(c). The peak positions of the t_{2g} and e_g states, which are the main sources of the magnetism of $MnSe_2$, rarely changed in the DOS. The electronic structure of the BT substrate adjacent to $MnSe_2$ is also well preserved. As expected based on Fig. 5(a), the BT layers become slightly p doped, merely shifting the Fermi level downward by approximately 0.1 eV without changing the overall shape of the DOS—see Fig. 5(d). Figure 5(e) shows that the T_C is enhanced by the topologically insulating BT substrate, but the presence of TSS is less relevant to the increase in the T_C. Because TSSs

start to appear in four or more quintuple layers (QLs) [60], the T_C enhancement observed in thin layers (<4 QL) is not related to the exchange mechanism intermediated by robust TSSs [61]. The calculated T_C is almost constant regardless of the BT thickness, implying the unrelatedness of the TSS of BT and the T_C enhancement. In addition, although SOC is a prerequisite for the realization of TSS, the T_C is well maintained, even in the absence of SOC (blue-filled boxes). The results clearly show that the T_C of $MnSe_2$ increases on top of a topological insulating BT substrate, but the enhancement is not driven by the TSS-mediated exchange mechanism but by the charge redistribution and additional exchange channel through the BT interface.

IV. CONCLUSION

The electronic and magnetic properties of the 2D FM $MnSe_2$ monolayer were investigated using DFT calculations. The calculated T_C of $MnSe_2$ varied with the on-site Coulomb repulsion parameter U. The optimal U value (3 eV) was chosen to reproduce the electronic and magnetic structures computed using the HSE hybrid functional. It was found that the T_C of pristine $MnSe_2$ is less than room temperature; however, in experiments, it can be increased by easily achievable variations, such as charge (electron or hole) doping and heterostructure engineering. Furthermore, the essential reasons for the T_C enhancement were identified in various heterostructures, such as $MnSe_2$/graphene, $MnSe_2$/GaSe, and $MnSe_2$/BT. Heterostructure engineering triggers the in-plane symmetry breaking and opening new additional exchange channels, which enhances the T_C. Unlike the close relation between the electronic correlations and the T_C of the monolayer $MnSe_2$, charge doping and heterostructure engineering are not directly related to the electronic correlation effect. Based on the fundamental understanding of the exchange mechanism in the $MnSe_2$ monolayer, practical guidelines were provided for tailoring the magnetic properties of 2D ferromagnets.

[1] J. F. Sierra, J. Fabian, R. K. Kawakami, S. Roche, and S. O. Valenzuela, Nat. Nanotechnol. **16**, 856 (2021).

[2] W. Yan, O. Txoperena, R. Llopis, H. Dery, L. E. Hueso, and F. Casanova, Nat. Commun. **7**, 13372 (2016).

[3] X. Lin, W. Yang, K. L. Wang, and W. Zhao, Nat. Electron. **2**, 274 (2019).

[4] D. Pesin and A. H. MacDonald, Nature Mater. **11**, 409 (2012).

[5] C. Gong, L. Li, Z. Li, H. Ji, A. Stern, Y. Xia, T. Cao, W. Bao, C. Wang, Y. Wang, Z. Q. Qiu, R. J. Cava, S. G. Louie, J. Xia, and X. Zhang, Nature (London) **546**, 265 (2017).

[6] Z. Fei, B. Huang, P. Malinowski, W. Wang, T. Song, J. Sanchez, W. Yao, D. Xiao, X. Zhu, A. F. May, W. Wu, D. H. Cobden, J.-H. Chu, and X. Xu, Nature Mater. **17**, 778 (2018).

[7] B. Huang, G. Clark, E. Navarro-Moratalla, D. R. Klein, R. Cheng, K. L. Seyler, D. Zhong, E. Schmidgall, M. A. McGuire, D. H. Cobden, W. Yao, D. Xiao, P. Jarillo-Herrero, and X. Xu, Nature (London) **546**, 270 (2017).

[8] M. Bonilla, S. Kolekar, Y. Ma, H. C. Diaz, V. Kalappattil, R. Das, T. Eggers, H. R. Gutierrez, M.-H. Phan, and M. Batzill, Nat. Nanotechnol. **13**, 289 (2018).

[9] A. Banerjee, J. Yan, J. Knolle, C. A. Bridges, M. B. Stone, M. D. Lumsden, D. G. Mandrus, D. A. Tennant, R. Moessner, and S. E. Nagler, Science **356**, 1055 (2017).

[10] Z. Zhang, J. Shang, C. Jiang, A. Rasmita, W. Gao, and T. Yu, Nano Lett. **19**, 3138 (2019).

[11] K. Kim, J. Seo, E. Lee, K.-T. Ko, B. S. Kim, B. G. Jang, J. M. Ok, J. Lee, Y. J. Jo, W. Kang, J. H. Shim, C. Kim, H. W. Yeom, B. Il Min, B.-J. Yang, and J. S. Kim, Nature Mater. **17**, 794 (2018).

[12] J. Seo, D. Y. Kim, E. S. An, K. Kim, G.-Y. Kim, S.-Y. Hwang, D. W. Kim, B. G. Jang, H. Kim, G. Eom, S. Y. Seo, R. Stania, M. Muntwiler, J. Lee, K. Watanabe, T. Taniguchi, Y. J. Jo, J. Lee, B. I. Min, M. H. Jo, H. W. Yeom, S.-Y. Choi, J. H. Shim, and J. S. Kim, Sci. Adv. **6**, eaay8912 (2020).

[13] A. F. May, D. Ovchinnikov, Q. Zheng, R. Hermann, S. Calder, B. Huang, Z. Fei, Y. Liu, X. Xu, and M. A. McGuire, ACS Nano **13**, 4436 (2019).

[14] N. Sivadas, S. Okamoto, X. Xu, Craig. J. Fennie, and D. Xiao, Nano Lett. **18**, 7658 (2018).

[15] Y. Liu, L. Wu, X. Tong, J. Li, J. Tao, Y. Zhu, and C. Petrovic, Sci. Rep. **9**, 13599 (2019).

[16] B. Huang, G. Clark, D. R. Klein, D. MacNeill, E. Navarro-Moratalla, K. L. Seyler, N. Wilson, M. A. McGuire, D. H. Cobden, D. Xiao, W. Yao, P. Jarillo-Herrero, and X. Xu, Nat. Nanotechnol. **13**, 544 (2018).

[17] S. Jiang, J. Shan, and K. F. Mak, Nature Mater. **17**, 406 (2018).

[18] C.-J. Kang, J. Hong, and J. Kim, J. Korean Phys. Soc. **80**, 1071 (2022).

[19] J.-U. Lee, S. Lee, J. H. Ryoo, S. Kang, T. Y. Kim, P. Kim, C.-H. Park, J.-G. Park, and H. Cheong, Nano Lett. **16**, 7433 (2016).

[20] K. Kim, S. Y. Lim, J. Kim, J.-U. Lee, S. Lee, P. Kim, K. Park, S. Son, C.-H. Park, J.-G. Park, and H. Cheong, 2D Mater. **6**, 041001 (2019).

[21] X. Cai, T. Song, N. P. Wilson, G. Clark, M. He, X. Zhang, T. Taniguchi, K. Watanabe, W. Yao, D. Xiao, M. A. McGuire, D. H. Cobden, and X. Xu, Nano Lett. **19**, 3993 (2019).

[22] S. Y. Kim, T. Y. Kim, L. J. Sandilands, S. Sinn, M.-C. Lee, J. Son, S. Lee, K.-Y. Choi, W. Kim, B.-G. Park, C. Jeon, H.-D. Kim, C.-H. Park, J.-G. Park, S. J. Moon, and T. W. Noh, Phys. Rev. Lett. **120**, 136402 (2018).

[23] S. Kang, K. Kim, B. H. Kim, J. Kim, K. I. Sim, J.-U. Lee, S. Lee, K. Park, S. Yun, T. Kim, A. Nag, A. Walters, M. Garcia-Fernandez, J. Li, L. Chapon, K.-J. Zhou, Y.-W. Son, J. H. Kim, H. Cheong, and J.-G. Park, Nature (London) **583**, 785 (2020).

[24] Q. Song, C. A. Occhialini, E. Ergeçen, B. Ilyas, D. Amoroso, P. Barone, J. Kapeghian, K. Watanabe, T. Taniguchi, A. S. Botana, S. Picozzi, N. Gedik, and R. Comin, Nature (London) **602**, 601 (2022).

[25] X. Zhang, Q. Lu, W. Liu, W. Niu, J. Sun, J. Cook, M. Vaninger, P. F. Miceli, D. J. Singh, S.-W. Lian, T.-R. Chang, X. He, J. Du, L. He, R. Zhang, G. Bian, and Y. Xu, Nat. Commun. **12**, 2492 (2021).

[26] C. Ataca, H. Şahin, and S. Ciraci, J. Phys. Chem. C **116**, 8983 (2012).

[27] M. Kan, S. Adhikari, and Q. Sun, Phys. Chem. Chem. Phys. **16**, 4990 (2014).

[28] I. Eren, F. Iyikanat, and H. Sahin, Phys. Chem. Chem. Phys. **21**, 16718 (2019).

[29] W.-Q. Xie, Z.-W. Lu, C.-C. He, X.-B. Yang, and Y.-J. Zhao, J. Phys.: Condens. Matter **33**, 215803 (2021).

[30] Q. Li, C. Zhang, D. Wang, K.-Q. Chen, and L.-M. Tang, Mater. Adv. **3**, 2927 (2022).

[31] P. Amiri, S. J. Hashemifar, and H. Akbarzadeh, Phys. Rev. B **83**, 165424 (2011).

[32] P. E. Blöchl, Phys. Rev. B **50**, 17953 (1994).

[33] G. Kresse and D. Joubert, Phys. Rev. B **59**, 1758 (1999).

[34] G. Kresse and J. Furthmüller, Phys. Rev. B **54**, 11169 (1996).

[35] J. P. Perdew, K. Burke, and M. Ernzerhof, Phys. Rev. Lett. **77**, 3865 (1996).

[36] V. I. Anisimov, F. Aryasetiawan, and A. I. Lichtenstein, J. Phys.: Condens. Matter **9**, 767 (1997).

[37] S. L. Dudarev, G. A. Botton, S. Y. Savrasov, C. J. Humphreys, and A. P. Sutton, Phys. Rev. B **57**, 1505 (1998).

[38] J. Heyd, G. E. Scuseria, and M. Ernzerhof, J. Chem. Phys. **118**, 8207 (2003).

[39] A. V. Krukau, O. A. Vydrov, A. F. Izmaylov, and G. E. Scuseria, J. Chem. Phys. **125**, 224106 (2006).

[40] S. Grimme, J. Comput. Chem. **25**, 1463 (2004).

[41] A. A. Mostofi, J. R. Yates, G. Pizzi, Y.-S. Lee, I. Souza, D. Vanderbilt, and N. Marzari, Comput. Phys. Commun. **185**, 2309 (2014).

[42] X. He, N. Helbig, M. J. Verstraete, and E. Bousquet, Comput. Phys. Commun. **264**, 107938 (2021).

[43] N. Marzari, A. A. Mostofi, J. R. Yates, I. Souza, and D. Vanderbilt, Rev. Mod. Phys. **84**, 1419 (2012).

[44] H. Xiang, C. Lee, H.-J. Koo, X. Gong, and M.-H. Whangbo, Dalton Trans. **42**, 823 (2013).

[45] D. J. O'Hara, T. Zhu, A. S. Ahmed, Y. K. Luo, C. H. Lee, M. R. Brenner, S. Rajan, J. A. Gupta, D. W. McComb, and R. K. Kawakami, Nano Lett. **18**, 3125 (2018).

[46] M. Wu, Y. Xiong, N. Jiang, M. Ning, and Q. Chen, J. Cryst. Growth **262**, 567 (2004).

[47] M. I. Katsnelson and A. I. Lichtenstein, Phys. Rev. B **61**, 8906 (2000).

[48] H. Wang, F. Fan, S. Zhu, and H. Wu, Europhys. Lett. **114**, 47001 (2016).

[49] K. Yang, F. Fan, H. Wang, D. I. Khomskii, and H. Wu, Phys. Rev. B **101**, 100402(R) (2020).

[50] H. L. Zhuang and R. G. Hennig, Phys. Rev. B **93**, 054429 (2016).

[51] Y. Sun, R. C. Xiao, G. T. Lin, R. R. Zhang, L. S. Ling, Z. W. Ma, X. Luo, W. J. Lu, Y. P. Sun, and Z. G. Sheng, Appl. Phys. Lett. **112**, 072409 (2018).

[52] J. Xiao, D. Legut, W. Luo, H. Guo, X. Liu, R. Zhang, and Q. Zhang, Phys. Rev. B **101**, 014431 (2020).

[53] J. Kim, K.-W. Kim, B. Kim, C.-J. Kang, D. Shin, S.-H. Lee, B.-C. Min, and N. Park, Nano Lett. **20**, 929 (2020).

[54] S. W. Jang, M. Y. Jeong, H. Yoon, S. Ryee, and M. J. Han, Phys. Rev. Mater. **3**, 031001(R) (2019).

[55] J. Kim, S.-H. Jhi, A. H. MacDonald, and R. Wu, Phys. Rev. B **96**, 140410(R) (2017).

[56] J. Kim and S.-H. Jhi, Phys. Rev. B **92**, 104405 (2015).

[57] S. Chen, C. Huang, H. Sun, J. Ding, P. Jena, and E. Kan, J. Phys. Chem. C **123**, 17987 (2019).

[58] J. Kim, K.-W. Kim, H. Wang, J. Sinova, and R. Wu, Phys. Rev. Lett. **119**, 027201 (2017).

[59] H. Wang, Y. Liu, P. Wu, W. Hou, Y. Jiang, X. Li, C. Pandey, D. Chen, Q. Yang, H. Wang, D. Wei, N. Lei, W. Kang, L. Wen, T. Nie, W. Zhao, and K. L. Wang, ACS Nano **14**, 10045 (2020).

[60] O. V. Yazyev, J. E. Moore, and S. G. Louie, Phys. Rev. Lett. **105**, 266806 (2010).

[61] Given that the T_C (or exchange constant) is less dependent on the thickness up to four quintuple layers, the T_C would be almost the same even in thicker Bi_2Te_3 because its surface electronic structure is not much different from that of four quintuple-layer Bi_2Te_3.